Synthesis of Novel Regenerable 13X Zeolite-Polyimide Adsorbent Foams

Ramya G[1,*], Barry Crittenden[1], Martin Smith[2], Olivier Camus[1], Y. M. John Chew[1], Semali Perera[1,*]

[1]Centre for Advanced Separations Engineering, Department of Chemical Engineering, University of Bath, Claverton Down, Bath BA2 7AY, UK

[2]CBR Division, Dstl Porton Down, Salisbury, SP4 0JQ, UK

*Correspondence: rg377@bath.ac.uk; S.Perera@bath.ac.uk;

Abstract

A new generic synthesis method is presented for the production of a polyimide (PI)/adsorbent (80 wt% 13X zeolite) regenerable foam filter. The method uses a dual parallel reaction foaming process comprising CO_2 generation (blowing) and polymerisation reactions. The paper describes the development of the foam structure and its characterisation in the context of removing CO_2 from air. Polyvinylpyrrolidone (PVP) of different molecular weights (10k, 40k and 58k) was used as a pore former to allow more adsorption sites to be exposed to CO_2. In dynamic adsorption breakthrough experiments at 101.325 kPa and 293 K, 10k PVP foams demonstrated an equilibrium loading of 0.039 g g^{-1} for CO_2 (at 40,000 ppmv in air), showing the best equilibrium time and adsorption capacity. The foams and equivalent commercial 13X beads were able to achieve loadings of 0.094 g g^{-1} and 0.097 g g^{-1} (at 40 mbar), respectively, when tested using pure CO_2 in an Intelligent Gravimetric Analyser. At pressures beyond 100 mbar, a weighted average isotherm shows only a 1.3 wt % reduction in adsorption capacity due to the polymer binder. The foams showed superior CO_2/N_2 selectivity compared to other adsorbents in literature. The thermal analysis of pure PI and 13X powder showed that the foams can be regenerated at 300°C. Computational Fluid Dynamics simulation was successfully implemented in order to understand the CO_2 adsorption behaviour on the new foam filter. Such modelling proved to be invaluable in understanding adsorptive behaviour through the complex foam structures as this is difficult to achieve experimentally.

Keywords

Adsorbent Foam; Polyimide; Adsorption; Isotherms; Modelling; Air filters

Nomenclature

Roman

Symbol	Definition	Units
A'	Coefficient for calculating k'_K	-
C	CO_2 concentration	mol m^{-3}
C_0	Initial Adsorptive Concentration	mol m^{-3}
C_t	Effluent Adsorptive Concentration at time t	mol m^{-3}
D	Diameter of foam	m
D_{CO_2}	CO_2 diffusion coefficient	m^2 s^{-1}
D_D	Dispersion tensor of CO_2	m^2 s^{-1}
D_e	Effective diffusion coefficient of CO_2	m^2 s^{-1}
D_L	Axial dispersion coefficient of CO_2	m^2 s^{-1}
D_p	Pore diameter	m
D_w	Pore-window diameter	m
F	Molar Flow Rate of CO_2	mol s^{-1}
H	Cell size	m
K	Permeability of porous domain	m^2
k'_K	Modified Kozeny constant	-
k_L	Langmuir constant	m^3 mol^{-1}
L	Length of foam	m or cm
m	Dry Adsorbent Weight	g
M_w	Molar Mass of CO_2	g mol^{-1}
$\boldsymbol{n}$	Flux vector	mol m^{-2} s^{-1}
P	Pressure	Pa

Pe	Peclet Number	-
Q	Volumetric flow rate of CO_2	$m^3\ s^{-1}$ or $mL\ min^{-1}$
q_b	Breakthrough Loading of CO_2	g CO_2 g^{-1} 13X Zeolite
q_{eq}	Equilibrium Loading of CO_2	g CO_2 g^{-1} 13X Zeolite
q_{max}	Maximum adsorption capacity	mol CO_2 g^{-1} 13X Zeolite
q_{eq,N_2}	Equilibrium Loading of N_2	g N_2 g^{-1} 13X Zeolite
r	Radial direction	m
Re_m	Modified Reynolds Number	-
Sc	Schmidt Number	-
S_{CO_2/N_2}	CO_2/N_2 Selectivity	-
T	Temperature	K
t	Time	s
t_b	Breakthrough Time	s
t_{eq}	Equilibrium Time	s
$\boldsymbol{u}$	Velocity vector	$m\ s^{-1}$
u_m	Mean fluid velocity	$m\ s^{-1}$
u_{max}	Maximum fluid velocity	$m\ s^{-1}$
u_z	Fluid velocity in axial direction	$m\ s^{-1}$
W	Radius of foam	m
y_{CO_2}	Molar fraction of CO_2	-
y_{N_2}	Molar fraction of N_2	-
z	Axial direction	m

Greek

Symbol	Definition	Units
ε_p	Foam voidage	-

μ_f	Viscosity of CO_2	Pa s
ρ_b	Bulk density	kg m^{-3}
ρ_f	Density of CO_2	kg m^{-3}
ρ_p	Polyimide density	kg m^{-3}
τ_f	Tortuosity factor	-
η	Cell ratio	-

1 Introduction

Zeolites and many other adsorbents are produced in powder form and engineered in the form of beads, granules or extrudates for conventional gas adsorption systems. These adsorbents require a binder to provide mechanical strength and macroporous structure for access to their active sites [1]. The particles, consisting of 15-20 w/w% binder, are commonly contained in packed beds, which are cost effective and versatile. According to many experts, the adsorption performance of packed beds, however, is far from optimised and often incurs significant pressure drop as well as high mass transfer resistances [2,3]. Attrition of particles could also occur due to the movement of the particles in the packed beds or during pressurisation-depressurisation steps. Uneven gas flow distribution through the bed can also contribute to poor performance of a packed bed [4,5]. It is very clear that there are many opportunities for the improvement and optimisation of adsorptive gas separation processes which should include the development of improved structured adsorbents [6].

To address the above issues, adsorbent structures such as nanotubes, fibres, laminates and monoliths have gained considerable interest as they enable immobilisation of particles to polymeric binding materials. The addition of an adsorptive filler to a polymeric membrane has been demonstrated to be an effective way of improving performance by enhancing sorption capacity for one or more of the compounds to be separated [7]. Parallel channel monolithic structures with controllable shape, cell density and wall thickness offer low pressure drop operation and higher mass transfer rates [8]. Pressure drop through monoliths is typically three to five times lower than that in a pellet system [9], although

the mass transfer characteristics of monoliths have been reported to be inferior compared to packed beds [10]. Monoliths with a high cell density provide a better separation performance but such a design becomes complex and thus difficult and expensive to manufacture [6].

Use of adsorbents in foam form is a relatively novel development [6]. Unlike monoliths, adsorbent foam structures can be manufactured and tailored into a wide variety of shapes, as they are not limited by the geometry of the extrusion die [11]. Although research has been carried out on adsorbent polyimide (PI) membranes, limited research has been reported on adsorbent polymeric foams [12]. Although foams are sponge-like structures with high porosity, the amount of adsorbent material in them may not be sufficient to exhibit the same volume activity as packed beds [6]. To overcome this issue, Yoon et al [13], reported a hydrothermal synthesis method of growing zeolite crystals within a macroporous structure, and thereby made the adsorbent surface accessible.

Ceramic foams are used for catalytic applications. Generally, these are either alumina or metallic and hence they are suitable for high temperature, abrasive and severely corrosive applications as a result of their high thermal and chemical stability [14]. Nonetheless, ceramic foams are disadvantageous as the manufacturing process is time-consuming and requires substantial heating at high temperatures for the calcining-sintering which can reach temperatures up to 1000℃ and the need for impregnation of chemical precursors for adsorbent encapsulation [15]. Polymeric/adsorbent composite foams, on the other hand, can be synthesized into any geometrical shape at room temperature via a simple process comprising of two parallel reactions [11,16]. Therefore, this paper concentrates on the development of a highly loaded adsorbent foam structure by manipulating the adsorbent content, the pore-former such as polyvinylpyrrolidone (PVP), the composition and the reaction conditions thereby creating the potential to increase the adsorbent content and the mass transfer in the foams compared to other adsorbent structures. An example model adsorbent selected for this research was commercially available 13X zeolite.

The criteria for selecting a suitable polymer is that it should be thermally stable at temperatures higher than 300℃ (used for regeneration), have good mechanical strength and have low foam manufacturing cost. PI and polybenzimidazole (PBI) are typical examples of commercial polymers which can be used

as a potential binder for foam filters because of their high mechanical strength and thermal stability [17]. A pure PI foam has been described by Liu et al [18]. The preparation of PBI foams would involve the addition of sulfuric acid to a PBI solution and heating up to temperatures of about 350 – 600°C [19]. More importantly, PI is reported to have excellent CO_2 solution-diffusion properties and permeation transport [20], and provides a class of amorphous high performance polymers characterised by excellent thermal properties and resistance to inorganic acids and bases [21]. Hence, PI was selected for producing the adsorbent foams in this work. A main challenge of this research is to ensure that embedded zeolite crystals provide the access to adsorb molecules such as CO_2, while retaining thermal stability for regeneration.

This paper presents the research and development of regenerable 13X zeolite/PI foam structures which have high adsorption capacity. The CO_2 adsorption performance of the foams and the effect of PI on the adsorption performance have been quantified using dynamic adsorption flow breakthrough curves and intelligent gravimetric analyser (IGA) adsorption isotherms. The thermal stability of the foam structures has been analysed using a thermogravimetric analyser (TGA), in order to select a suitable regeneration temperature. Alongside the experimental work, numerical modelling has been used to elucidate the mass transfer characteristics of CO_2 through the foams including the adsorption of CO_2 onto the surface of the immobilised 13X zeolite.

2 Materials and Methods

2.1 Materials

Pyromellitic dianhydride (97%, PMDA), 1-methyl-2-pyrrolidone (Reagent grade, 99%, NMP), silicon oil (viscosity 350 cSt), ethanolamine (Amine Catalyst), dibutyltin dilaurate (Tin Catalyst), poly [(phenyl isocyanate)-co-formaldehyde] (Isocyanate) and polyvinylpyrrolidone (PVP) with molar mass of 10000 Da (10k), 40000 Da (40k) and 58000 Da (58k) were all supplied by Sigma-Aldrich. Adsorbent 13X powder was supplied by Honeywell UOP (HU), Air Products (AP) and Zeochem (ZC). The adsorptive gas for adsorption experiments was CO_2 (40000 ppmv/4% vol.) in air and was supplied by BOC Ltd. (UK).

2.2 Preparation of 20 wt% PI/ 80 wt% 13X Foams

The first mixture (as shown in Figure 1) was prepared by mixing PMDA:NMP (1:8.4), distilled water (10 – 15 mL), amine catalyst (~50 µL), silicon oil (1 – 2 g) and PVP (5 wt% based on PMDA/Isocyanate content) using a homogeniser at 6500 rpm for 30 seconds. Then 13X (40 g), additional NMP (20 – 30 mL) and tin catalyst (~25 µL) were added to the mixture and stirred using a homogeniser at 6500 rpm for 30 seconds to generate the second mixture (see Figure 1). The second mixture was then added to 5 g of isocyanate and mixed using the homogenizer at 6500 rpm for 5 seconds. During the last mixing step, the PI foaming process begins and this involves the 'blowing' and polymerization reactions taking place simultaneously. During the blowing reaction, isocyanate reacts with the distilled water to produce CO_2 and a primary amine to create pores in the foam. The importance of the presence of water during the foaming process can be seen in Table 1. Small air bubbles that were created during mixing serve as nucleation sites for the CO_2. The CO_2 diffuses into the small air bubbles and as more CO_2 is generated, the bubbles expand and the foam starts to rise. The amine catalyst controls the reaction between the isocyanate group and water. At the same time, in the polymerization reaction, the primary amine reacts with PMDA to produce an amic-acid which subsequently imidizes to produce an imide whilst regenerating water at the same time. During this reaction, gas-filled cells with thin walls are formed. This polymerization reaction is catalysed by the tin catalyst [22–25]. The foaming process takes approximately 10 – 15 seconds for the mixture to rise and polymerize. The polymerized PI foam was then obtained by washing, soaking in a water bath and drying in an oven at 100°C till no change in foam weight was observed.

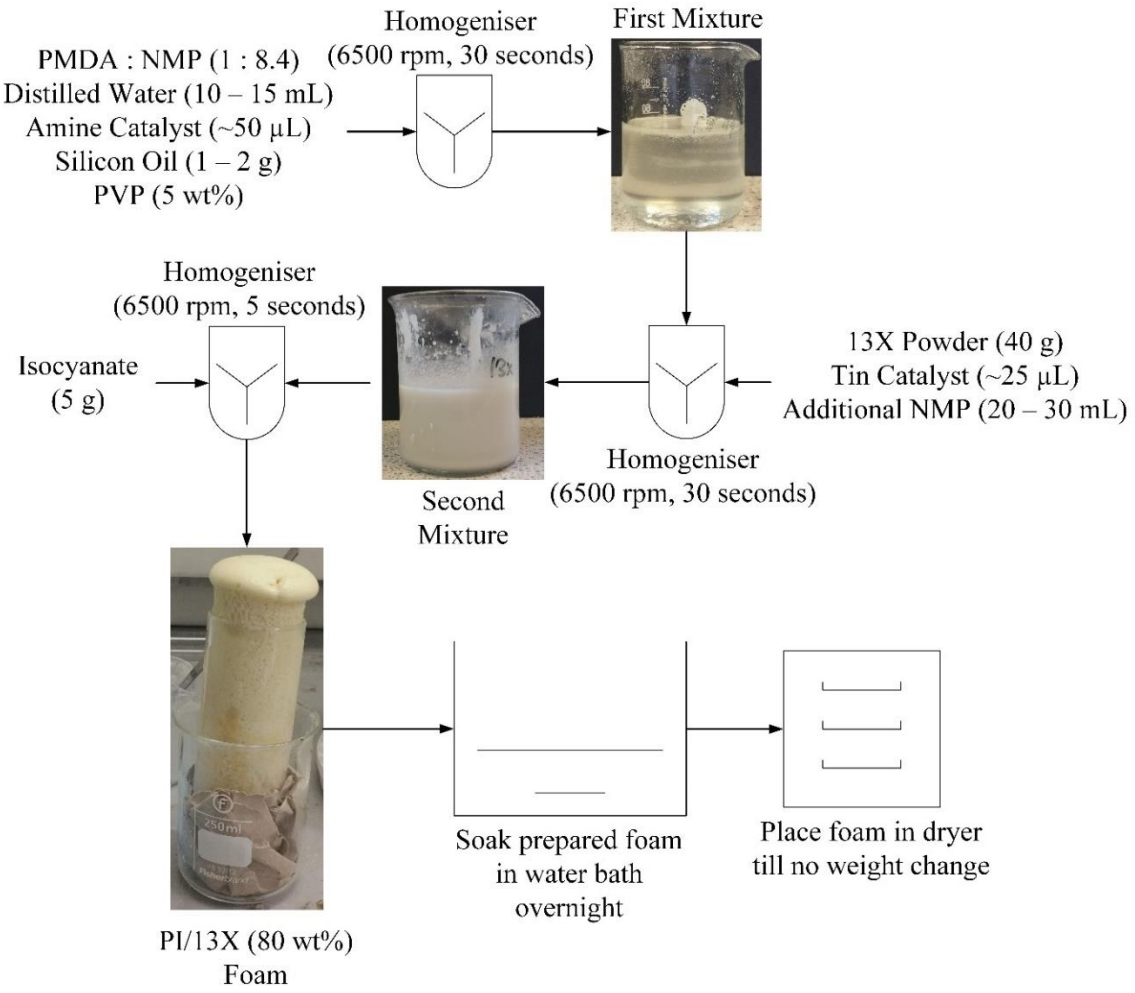

Figure 1: Method of preparing a PI/13X (80 wt%) Foam.

Table 1: Amount of water content for the fabrication of PI/13X zeolite foams.

	Figure 3 (a) PI/13X (AP) foam	Figure 3 (b) PI/13X (ZC) foam	Figure 3 (c) PI/13X (HU) foam	Figure 3 (d) PI/13X (ZC, dried) foam	Figure 3 (e) PI/13X (HU) foam after water content adjustment
Zeolite powder treatment prior to foaming	None	None	None	Dried in oven at 300°C for 24 hours	None

Water content in zeolite powder	24.8%	19%	0%	0%	0%
Water content (mL)	0.5 – 1*				10 – 15*
Zeolite content	80 wt%				
PI content	20 wt%				

* Water content recommended for saturating the zeolite (may vary based on type of zeolite used) as well as for the foaming process

In addition to the existing pores created by the blowing reaction, PVP was added as a pore former to further improve the accessibility of the adsorptive gas to the zeolite surface. The removal rate of PVP depends on its' molar mass and its' solubility in water. During the phase inversion and regeneration process, it is assumed that the PVP is removed from the foam.

2.3 Characterisation

2.3.1 Thermogravimetric Analyser (TGA)

A TGA (Setaram TG-92) was used to analyse the thermal properties of pure PI and pure 13X. A small alumina crucible was used to hold and weigh crushed samples on a microbalance in the insulated furnace at room temperature. Cool water was used to control the environment in the furnace and the system was purged using argon gas. The sample was then heated in nitrogen from 20 to 1000℃ at a rate of 10℃ min^{-1}. The temperature in the furnace was regulated by the built-in thermocouple. Using the same conditions, a blank thermogravimetry (TG) curve was generated with an empty alumina crucible as shown in Figure A. 1 (Appendix) and this was used to correct the TG measurements presented in this paper. The analyser was connected to a computer which recorded the changes in the mass of the sample at different temperatures using a programme called SetSoft2000. Once the analysis had completed, the sample was cooled to room temperature before removal from the furnace. From the recorded data, TG curves were obtained by plotting the change in the weight of the sample as a function of temperature and differential thermogravimetry (DTG) curves were obtained by plotting the derivative of the TG values, as a function of temperature.

2.3.2 Intelligent Gravimetric Analyser (IGA)

Pure CO_2 adsorption properties of pure 13X, PI/13X (80 wt%) and PI/13X (85 wt%) foams, 13X beads, pure PI and pure N_2 adsorption properties of PI/13X (80 wt%) foams were determined using a Hiden Intelligent Gravimetric Analyser (IGA-001). The sample (~100 mg) was crushed and loaded onto the sample holder and weighed using the built-in microbalance at room temperature and pressure. The reactor chamber was sealed and outgassed at a rate of 150 mbar min^{-1} to 10^{-6} mbar to ensure that there was no gas remaining in the chamber. All samples were pre-treated in the IGA by heating at 300°C for 10 hours under vacuum to remove water or gas contaminants that may have been present. The sample was then cooled to room temperature (20°C) and the dry mass of the sample was recorded. CO_2 adsorption isotherm data were obtained at 10 mbar increments up to 100 mbars, followed by 100 mbar increments up to 1 bar all at 20°C. During the isotherm measurements, the sample weight was recorded at each pressure point and allowed to equilibrate before moving to the next pressure point. Using the measured data, the equilibrium adsorption capacity of the samples was plotted as a function of pressure.

2.4 Dynamic Adsorption Experiments

A schematic diagram of the adsorption flow-breakthrough apparatus used to determine the adsorption properties of the PI/13X foams is shown in Figure 2. The apparatus consists of an adsorption column, feed gas flow system and a data logger for recording the CO_2 concentration in the gas stream exiting the adsorption column. The adsorption column was placed in a temperature-controlled cabinet. A sintered plate flow distributor was fitted prior to the inlet of the foam structure to help create a uniform flow distribution (at least at the inlet). A mass flow controller (MFC, Brooks Instruments, 0254) was used to control the feed flow rate of CO_2 to the column and to maintain the adsorption column at a constant pressure of 1 bar. An infrared gas instrument (Edinburgh Sensors) was used to monitor the column outlet CO_2 concentrations. The PI/13X foams were challenged with 4% vol. CO_2 in air for all adsorption experiments. The foams were regenerated at 300°C for 24 hours to examine the effect of heat cycles on the adsorption performance of the foams. Polytetrafluoroethylene (PTFE) tape was used to create a seal around the ends of each foam before placing inside the column to prevent gas leakage at the wall. This ensured that the CO_2 only flows through the foam and not around the foam wall. All

adsorption experiments were carried out with a feed gas flow rate of 500 mL min^{-1} and at room temperature (20°C) and pressure (1 bar). A stack of three foams (total height: 27 cm, diameter: 3.7 cm) with the same composition were used for each adsorption experiment as shown in Figure 2.

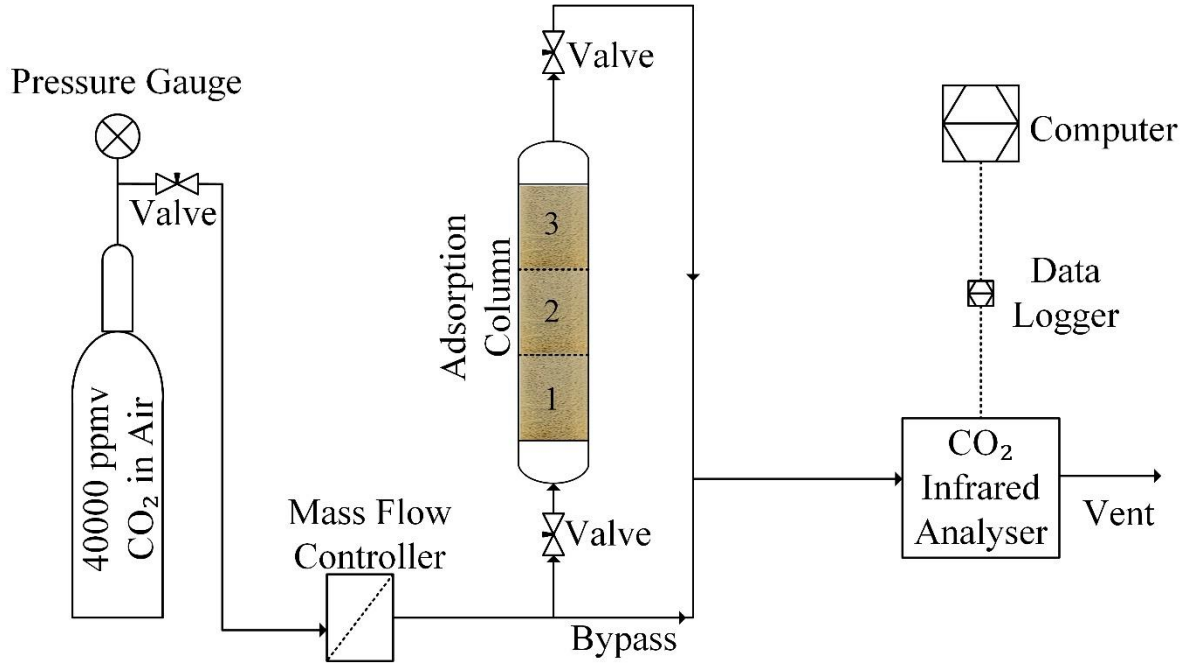

Figure 2: Schematic diagram of the CO_2 adsorption apparatus.

Breakthrough curves generated from the adsorption experiments were used to determine parameters such as breakthrough and equilibrium time as well as breakthrough and equilibrium loading. Breakthrough time, t_b, indicates when the filter is of no further use, equilibrium time, t_{eq}, indicates when the effluent concentration, C_t, is equal to the initial adsorptive concentration, C_0. The equilibrium loading, q_{eq} and breakthrough loading, q_b of the foams, were calculated using Equations 1 and 2 [26]:

$$q_{eq} = \frac{F \times M_w \times \left[t_{eq} - \int_0^{teq} \frac{C_t}{C_0} dt\right]}{m} \quad (1)$$

$$q_b = \frac{F \times M_w \times \left[t_b - \int_0^{t_b} \frac{C_t}{C_0} dt\right]}{m} \quad (2)$$

where F is the molar flowrate of adsorptive gas, M_w is the molar mass of adsorptive gas and m is the dry adsorbent weight. All calculations were performed on the assumption that all of the PVP had leached

out of the foam during the washing and processing stage. The PI/13X zeolite foam samples that were used for dynamic adsorption experiments are summarised in Table 2.

Table 2: Adsorption characterization of PI/13X zeolite foam samples, Legend: 300 indicates regeneration temperature, H indicates number of heat cycles and S indicates different foam samples with the same formulation.

CO_2 Adsorption Experiment (Section 3.3)				
Regeneration Temperature (℃)	PVP Molar Mass	Zeolite Content	PI Content	Sample Name
300	No PVP	80 wt%	20 wt%	300-0k, H1S1
				300-0k, H4S1
				300-0k, H8S1
				300-0k, H10S1
				300-0k, H4S2
	10k			300-10k
	40k			300-40k
	58k			300-58k

3 Results and Discussion

3.1 Fabrication of PI/13X Zeolite Foams

Table 1 and Figure 3 shows the importance of saturating the zeolite prior to the foaming process. The different batches of 13X zeolite supplied were dried in the furnace at 300℃ for 24 hours as shown in Table 1, to quantify the amount of water required for a generalised adsorbent foam formulation. Since 13X from AP and ZC were supplied saturated with moisture, significant weight losses of 24.8% and 19% respectively, were observed. Therefore, Figure 3 (a) and (b) shows that 0.5 – 1 mL of water was sufficient to produce the foams. However, 13X from HU was not saturated with moisture and thus showed no weight loss. Therefore, Figure 3 (c) shows that the same 0.5 – 1 mL of water had caused the foam to collapse on itself during the foaming process and become hard once it had dried. This may have

been the result of the water necessary for the blowing reaction having been adsorbed by the hydrophilic 13X. The lack of water necessary for the blowing reaction did not generate CO_2 and thus, the foams were hard. 13X from AP and ZC were used successfully to fabricate a foam. Therefore, 13X from ZC was dried at 300°C for 24 hours prior to making the foams to confirm the effect unsaturated zeolite had on the foaming process. Similar to the PI/13X (HU) foam, Figure 3 (d) shows that the foam had also collapsed when unsaturated 13X from ZC was used. In order to saturate 13X from HU prior to the foaming process, 10 – 15 mL of water was added as the water capacity of the 13X was found to be approximately 30 wt% of its dry weight [27]. Figure 3 (e) shows that with the addition of 10 – 15 mL of water, PI/13X foams containing 80 wt% of 13X, were successfully fabricated using the formulation described in Section 2.2. Since this was the best formulation, it was used to produce foams for all experiments in this study.

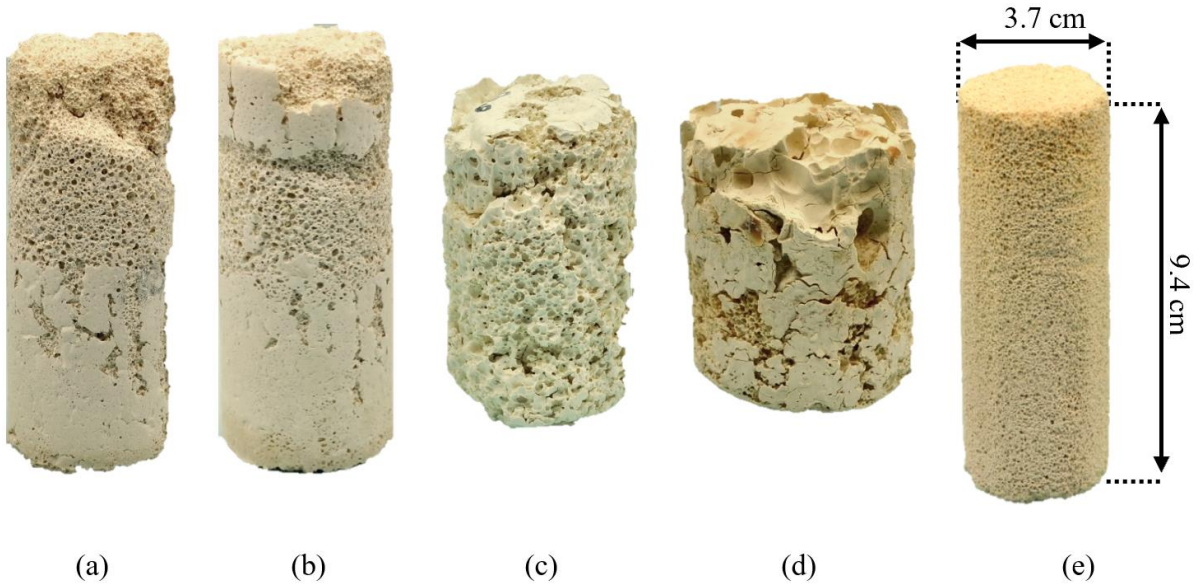

Figure 3: (a) PI/13X (AP) foam, (b) PI/13X (ZC) foam, (c) PI/13X (HU) foam, (d) PI/13X (ZC, dried) foam, (e) PI/13X (HU) foam after water content adjustment; PI/13X (HU) foams were used for all adsorption experiments.

3.2 Thermal Analysis of Pure PI and 13X Zeolite

A suitable regeneration temperature was determined from the analysis of the thermal stability of pure 13X powder and pure PI foam samples. The pure PI foam sample was prepared as stated in Section 2.2.

Figure 4 (a) and (b) shows the weight loss of pure 13X zeolite powder and pure PI foam as a function of temperature respectively. The DTG curve was used to examine for changes in the weight of the sample that were not distinctly shown on the TG curve. As a result of a clear slope observed for pure 13X in Figure 4 (a), the DTG curve was not plotted for the zeolite.

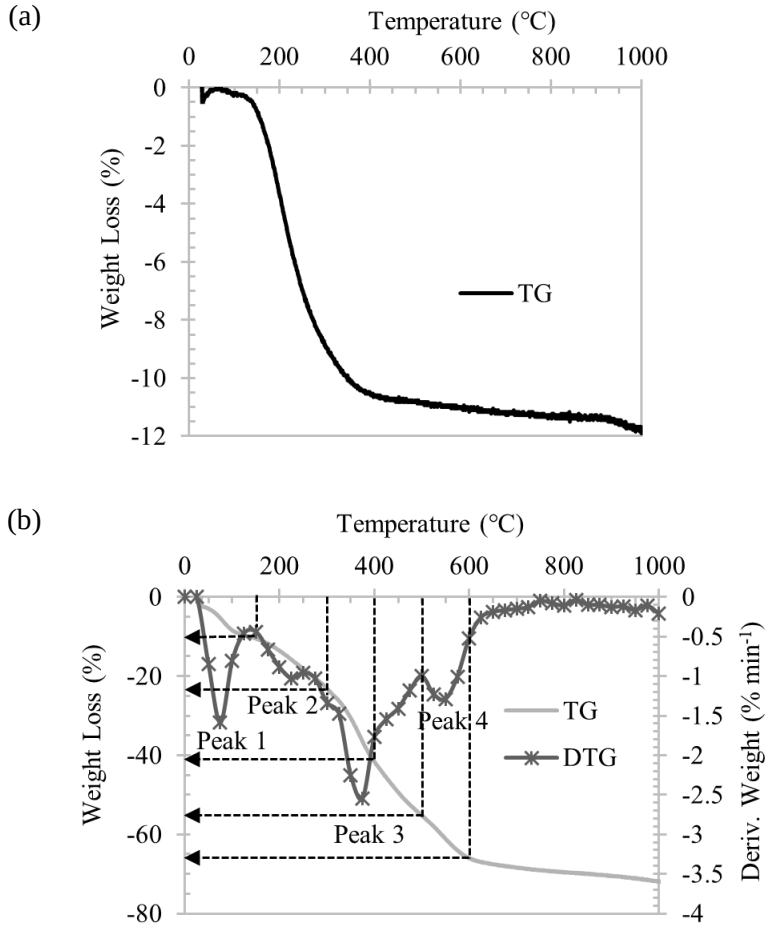

Figure 4: (a) Thermogravimetry (TG) curve of pure 13X zeolite powder, (b) Thermogravimetry – Differential Thermogravimetry (TG-DTG) curves of pure PI foam (Peak 1: 50 – 150°C, Peak 2: 150 – 300°C, Peak 3: 300 – 400°C, Peak 4: 500 – 600°C on DTG curve).

The TG curve of pure 13X powder plotted in Figure 4 (a) shows a weight loss of approximately 11% at 400°C. This was due to the loss of water that was adsorbed on the zeolite surface as well as present in the zeolite channels. Figure 4 (a) suggests that by 400°C, 13X had completely regenerated. These observations were confirmed by Zhou et al [28]. Since it is necessary to ensure that the PI will remain stable during the regeneration process, the thermal degradation of the pure PI foam sample was analysed

as shown in Figure 4 (b). The TG curve of the pure PI foam sample plotted in Figure 4 (b) shows a distinct weight loss of approximately 10% at 150℃ as a result of the removal of moisture from the sample. A significant weight loss is seen from 150℃ to 600℃. In order to identify the presence of overlapping weight loss, the DTG curve was plotted as shown in Figure 4 (b). Figure 4 (b) indicates four weight loss peaks at 50 – 150℃ (Peak 1), 150 – 300℃ (Peak 2), 300 – 400℃ (Peak 3) and 500 – 600℃ (Peak 4). Peak 2 that was observed in the DTG curve from 150 – 300℃, may be due to the removal of residual solvent (NMP) present in the pure PI foam sample as it has a boiling point of 204℃. A similar pattern was observed by Liu et al [18] when N, N-dimethyl formamide (DMF, solvent) was released at approximately 175℃ for a pure PI foam. At 300℃ and 400℃, the corresponding weight loss observed using the TG curve was approximately 25% and 40% of the original PI foam weight respectively. This may have been due to the release of small residual molecules such as O_2 and CO_2 and the thermal decomposition of unstable segments (urea bonds) in the foam. At 500℃ and 600℃, the PI foam had lost approximately 55% and 65% of its original weight respectively. This could have been due to the thermal pyrolysis of the imide ring in the rigid PI structure. Both these observations were confirmed by Yu et al [29] when they carried out a thermogravimetry-Fourier transform infrared spectroscopy analysis on a pure PI foam.

The criteria for selecting a suitable regeneration temperature is to avoid pyrolysis of the PI component in the foam whilst ensuring the regeneration of the 13X zeolite. 13X zeolites used in industry are regenerated at temperatures ranging from 204℃ to 316℃ for thermal swing cycles [27]. In order to avoid long periods of regeneration and the pyrolysis of the PI component in the foam, 300℃ was accordingly selected as a suitable regeneration temperature.

3.3 Effect of PVP Molar Mass on Adsorption Properties

(a)

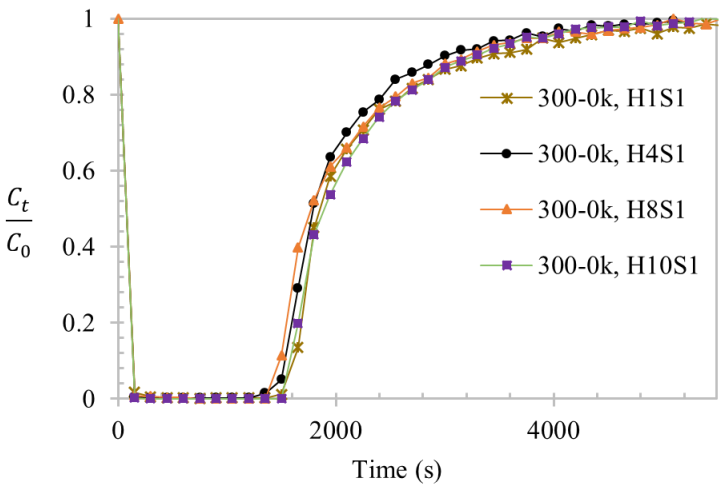

(b)

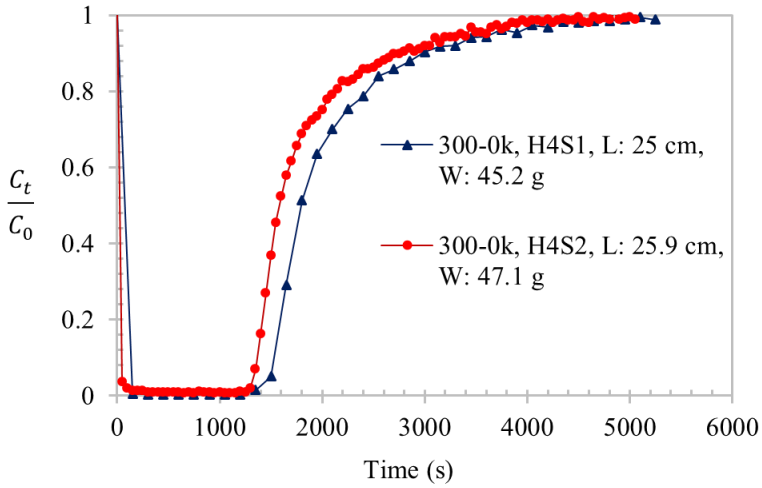

Figure 5: (a) Effect of number of heat cycles on adsorption breakthrough curve, (b) Repeatability of breakthrough curves using two different batches of 300-0k foams, Legend: L – Total length of three foams, W – Total weight of three foams, H – Number of heat cycles, S – Sample number.

Figure 5 and Figure 6 show the breakthrough curves obtained from running CO_2 adsorption experiments using the PI/13X foams. To examine the effect of heat cycles on the adsorption performance of the foams, the breakthrough curve obtained after one, four, eight and ten heat cycles were compared, as shown in Figure 5 (a). This shows that that there were negligible differences observed in the breakthrough curves. Repeatability of breakthrough curves using 300-0k H4S1 and 300-0k H4S2 are shown in Figure 5 (b). These two different samples with the same formulation were manufactured using the same foaming conditions. Both samples contain no PVP and were regenerated at 300°C prior to all

adsorption experiments. The discrepancies could be due to the slight variation between the samples. 4% vol. CO_2 adsorption breakthrough curves after four heat cycles using the four different PVP formulations after four heat cycles, are shown in Figure 6.

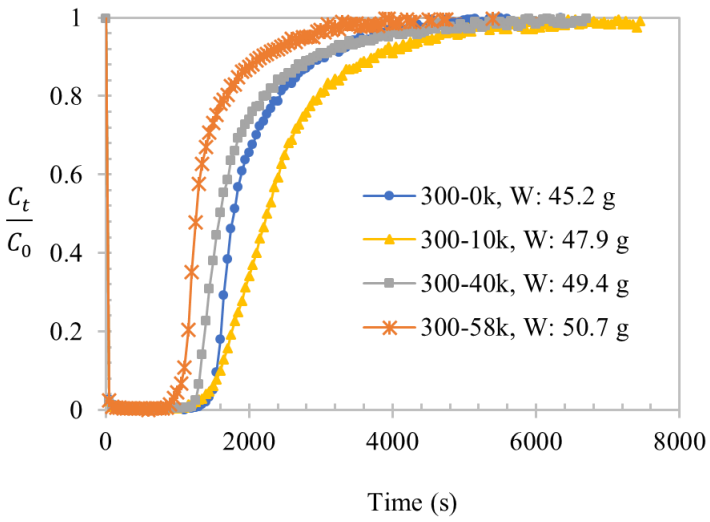

Figure 6: Comparison of adsorption breakthrough curves obtained with 4% vol. CO_2 in air challenge foams with 10k, 40k and 58k PVP pore former and without any PVP in the structure (after four heat cycles), Legend: W – Total weight of three foams.

The breakthrough data such as t_b and t_{eq}, were obtained from the breakthrough curves shown in Figure 6. t_b indicates the time point when CO_2 is detected at the outlet of the filter and t_{eq} indicates the time point when the filter has become saturated. q_{eq} and q_b, were calculated using Equations 1 and 2 and these results are presented in Table 3. t_b was selected when CO_2 concentration reached 1% of the initial concentration, C_0. t_{eq} was selected once a maximum of five consecutive C_0 readings had been achieved.

Table 3: Adsorption properties of PI/13X foams tested at 20℃ (Each sample regenerated at 300℃).

Sample	$t_b\ (s)$	$t_{eq}(s)$	$q_b\left(\frac{g\ CO_2}{g\ 13X}\right)$	$q_{eq}\left(\frac{g\ CO_2}{g\ 13X}\right)$
300-0k	1287 ± 0.5%	5195 ± 2.2%	0.021 ± 1.3%	0.032 ± 6.4%
300-10k	1144	7462	0.018	0.039
300-40k	1216	6738	0.018	0.029

300-58k	886	6692	0.013	0.021

Table 3 shows that the CO_2 breakthrough time for 10k PVP foams was 1144 s, compared to 1287 s for 300-0k. Therefore, the breakthrough loading for 10k PVP foams was 0.018 $g\ CO_2/g\ 13X$ and this was lower compared to 0.021 $g\ CO_2/g\ 13X$ for 300-0k. However, the equilibrium time for 10k PVP foams was 7462 s, compared to 5195 s for 300-0k. The equilibrium loading for 10k PVP foams was 0.039 $g\ CO_2/g\ 13X$ and this was higher compared to 0.032 $g\ CO_2/g\ 13X$ for 300-0k. This can be explained by PVP domains that are created throughout the PI matrix, as a result of the hydrophilic nature of PVP and the hydrophobic nature of PI [30]. In the presence of these domains, the diffusional pathway for the CO_2 molecules is enhanced. This shows that the 10k PVP foams adsorbed more CO_2 compared to 300-0k, as there is an improvement in the accessibility of the adsorptive molecules to the 13X active site. Unlike the improvement in the adsorption performance that the 10k PVP foams showed, the breakthrough and equilibrium loading of 40k PVP foams were 0.018 $g\ CO_2/g\ 13X$ and 0.029 $g\ CO_2/g\ 13X$ respectively, and the breakthrough and equilibrium loading of the 58k PVP foams were 0.013 $g\ CO_2/g\ 13X$ and 0.021 $g\ CO_2/g\ 13X$ respectively. Both the breakthrough and the equilibrium loadings were lower compared to 300-0k.

This may be a result of the 10k PVP having a lower retention factor (wt% of PVP remaining in the foam) due to a higher amount of PVP leaching out into the water bath during the pre-treatment washing process thus creating greater amount of skin porosity, compared to the 40k and 58k PVP. This observation was confirmed by an analysis that was done on a polysulfone membrane containing PVP by Matsuyama et al [31]. These results also suggest that the presence of high molar mass PVP in the foam might be causing some of the 13X adsorption sites to be covered and thereby reducing the adsorption capacity of the foams. Therefore, the 10k PVP foams had a higher adsorption loading compared to the 40k and 58k PVP foams as confirmed in Table 3.

3.4 IGA CO_2 Adsorption Isotherms

Since the adsorbent foams were composed of 20 wt% PI and 80 wt% 13X zeolite, there may be a possibility that PI could also mask the adsorbent active sites. As a model system of 4% vol. CO_2 in air

was used to challenge the PI/13X foam samples during the dynamic adsorption experiments, it is possible that N_2 adsorption could interfere with the adsorption of CO_2. PI/13X foams were tested to determine if there was interference to CO_2 adsorption caused by the presence of PI and N_2. Figure 7 presents the adsorption isotherms obtained using pure CO_2 for pure 13X, 300-10k (PI/13X (80 wt%)), Pure PI, PI/13X (85 wt%) and 13X beads (Park et al, [32]) and pure N_2 for 300-10k (PI/13X (80 wt%)). The CO_2 adsorption isotherm results of two different 10k PVP foam samples with the same formulation were represented as error bars, as shown in Figure 7.

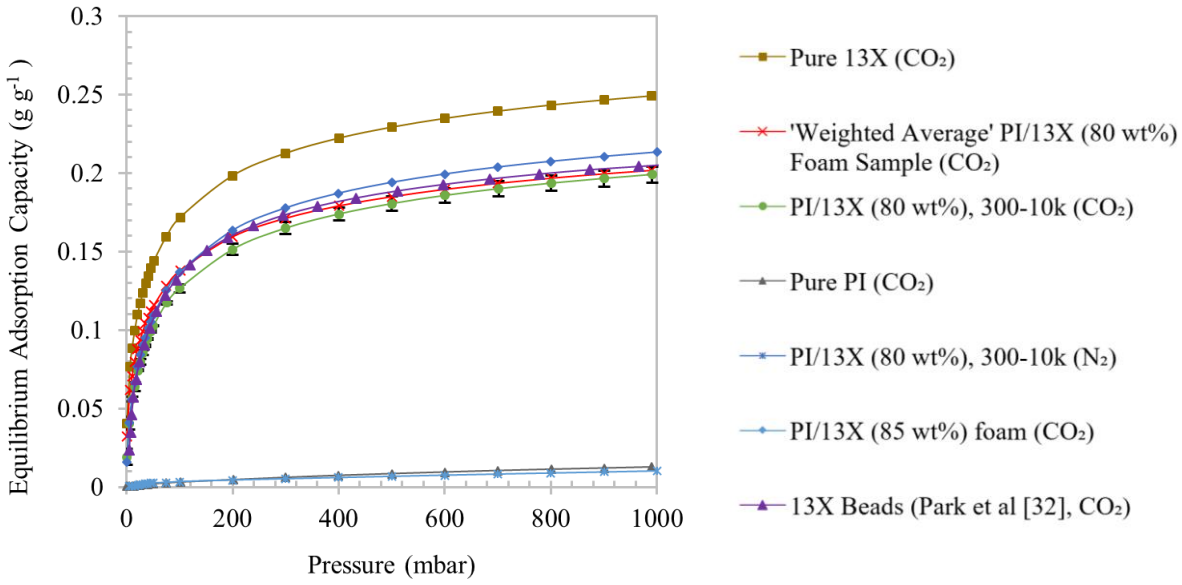

Figure 7: CO_2 adsorption isotherms of pure 13X, pure PI, 'Weighted Average' PI/13X (80 wt%) foam sample, 300-10k (PI/13X (80 wt%)) (n = 3), PI/13X (85 wt%) foam, 13X beads (Park et al, [32]) and 300-10k (N_2 adsorption isotherm) up to 1 bar at 20°C.

The CO_2 adsorption properties of pure 13X and a pure PI foam sample without any 13X, were determined using the IGA. An isotherm was then predicted for a PI/13X foam sample, by taking a weighted average of the pure 13X isotherm and the pure PI isotherm as shown in Equation 3. Since the actual PI/13X foam samples contain 80 wt% of 13X zeolite and 20 wt% of PI, the same composition was used to predict the 'weighted average' isotherm.

$$Weighted\ Average = (0.8 \times CO_2\ uptake\ by\ pure\ 13X) + (0.2 \times CO_2\ uptake\ by\ pure\ PI) \quad (3)$$

As shown in Figure 7, typical type I isotherms were observed for all the samples tested. This characteristic is typical of micro-porous materials. Figure 7 clearly shows that over the low-pressure range (0 – 100 mbar), CO_2 adsorption occurs rapidly and approaches equilibrium as the pressure continues to increase. Adsorption capacity of 300-10k (PI/13X (80 wt%)), increased from approximately 0.056 g g^{-1} at 10 mbar to 0.2 g g^{-1} at 1000 mbar. Similarly, adsorption capacity of pure 13X increased from 0.088 g g^{-1} at 10 mbar to 0.249 g g^{-1} at 1000 mbar.

With the pure PI foam, negligible uptake of CO_2 was observed. As expected, the adsorption isotherm obtained from the 10k PVP (PI/13X (80 wt%)) foam samples was lower compared to the pure 13X isotherm. Figure 7 shows that the 'Weighted Average' isotherm of the PI/13X (80 wt%) foam was slightly higher than the measured adsorption isotherm of 300-10k (PI/13X (80 wt%)). Hence, it is possible that some loss of adsorption capacity is observed as a result of masking by the polymer.

At 100 mbar, the adsorption capacity of the 'Weighted Average' isotherm was approximately 9% higher compared to the measured isotherm of 300-10k (PI/13X (80 wt%)). However, at pressures beyond 100 mbar, the adsorption capacity of the 'Weighted Average' isotherm was approximately 1.3% higher compared to the measured isotherm of 300-10k (PI/13X (80 wt%)). This suggests that by operating at higher concentrations, a higher adsorption capacity can be achieved due to more CO_2 molecules being attracted onto 13X zeolite. This similar trend was seen in a study that was carried out by Hauchlum and Mahanta [33] for commercial 13X powder at 25°C using 13.8 vol% CO_2 in air. However, the adsorption capacity obtained by Hauchlum and Mahanta was lower compared to the adsorption capacities observed in our study (Figure 7) due to the higher operating temperature and lower CO_2 concentration.

Figure 7 shows that the adsorption capacity of the PI/13X (85 wt%) foam sample increased from approximately 0.056 g g^{-1} at 10 mbar to 0.21 g g^{-1} at 1000 mbar. At a lower pressure (<100 mbar), the adsorption capacity of the PI/13X (85 wt%) foam sample was similar to 300-10k. However, as the pressure increased the difference in adsorption capacity between 300-10k (PI/13X (80 wt%)) and the PI/13X (85 wt%) foam sample increased by 0.01 g g^{-1}. However, this paper concentrated on PI/13X (80 wt%) foam since it is comparable to commercially supplied adsorbents (20 wt% binder/80 wt% 13X). The data presented for 13X beads in Figure 7 were obtained from Park et al [32]. The 13X beads had

an adsorption capacity of approximately 0.2 g g^{-1} at 100 kPa and this was similar to the adsorption capacity obtained by 300-10k (PI/13X (80 wt%)). This shows that both 300-10k (PI/13X (80 wt%)) and the commercial 13X beads exhibit an adsorption performance that is comparable to each other.

Unlike the CO_2 uptake observed with 300-10k (PI/13X (80 wt%)), the foam sample showed very low uptake of N_2 as seen in Figure 7. The ideal adsorption solution theory (IAST) was used to predict the CO_2/N_2 selectivity for a binary gas mixture [34]:

$$S_{CO_2/N_2} = \left(\frac{q_{eq}}{y_{CO_2}}\right) \Big/ \left(\frac{q_{eq,N_2}}{y_{N_2}}\right) \quad (4)$$

where S_{CO_2/N_2} is selectivity, q_{eq} and q_{eq,N_2} are equilibrium loading of CO_2 and N_2 respectively, y_{CO_2} and y_{N_2} are molar fractions of CO_2 and N_2.

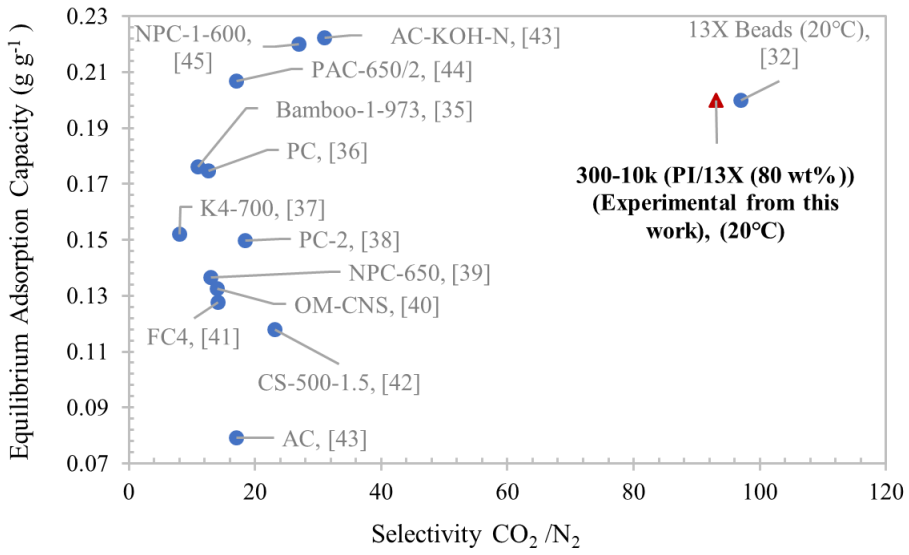

Figure 8: Comparison of equilibrium adsorption capacity and CO_2/N_2 selectivity of 300-10k (PI/13X (80 wt%)) foam with different adsorbents at 25°C (unless otherwise shown in the figure) and 1 bar for a flue gas mixture (85% N_2, 15% CO_2).

Figure 8 compares the adsorption performance and the CO_2/N_2 selectivity of 300-10k (PI/13X (80 wt%)) with other adsorbents from literature. Since the selectivity values of Bamboo-1-973 [35], PC [36], K4-700 [37], PC-2 [38], NPC-650 [39], OM-CNS [40], FC4 [41], CS-500-1.5 [42], AC [43], PAC650/2 [44], NPC-1-600 [45] and AC-KOH-N [43] were for a flue gas mixture (85% N_2, 15% CO_2),

the selectivity of 300-10k (PI/13X (80 wt%), this work) and the 13X beads (data obtained from Park et al [32]) were calculated for a flue gas mixture using Equation 4. As seen in Figure 8, most of the adsorbents obtained from literature had a lower adsorption capacity compared to 300-10k (PI/13X (80 wt%)) except for PAC650/2, NPC-1-600 and AC-KOH-N. However, all of the adsorbents had a lower selectivity compared to 300-10k (PI/13X (80 wt%)).

4 Numerical Modelling

A 2-dimensional axisymmetric model was developed and solved using a commercial package COMSOL Multi-Physics V5.3. Species and momentum conservation equations were coupled and solved to describe the transport of CO_2 through the foam as well as CO_2 adsorption throughout the foam.

4.1 Physical Model and Assumptions

The model foam system implemented in the computational fluid dynamics (CFD) consisted of a single foam with diameter, D of 0.037 m and length, L of 0.27 m. The flow rate of CO_2 in air, Q was set at 8.33×10^{-6} m^3 s^{-1} (500 mL min^{-1}), CO_2 concentration, C_0 was 4% vol. and the model was set to solve at temperature, T of 293.15 K and at pressure, P of 101325 Pa. These conditions were based on the conditions used in the dynamic flow experiments. The domain was assumed to be porous with voidage, ε_p and 13X zeolite was uniformly immobilized in the polymer matrix. A model representation of the experimental setup and the foams is shown in Figure 9 (a). Definition and values of the model input parameters and variables used in Section 4, is summarised in Table 4.

The assumptions used in the model were [46]:

- 2-D axisymmetric – since the pores in the foam structures were random as seen in Figure 9 (b), it was reasonable to assume that there was negligible variation of flow properties in the azimuthal direction.
- Negligible axial back mixing (Pe ~ 280 according to Equation 7)
- Permeability and porosity of the system is isotropic
- Negligible adsorption of the carrier gas (Negligible adsorption of N_2, Figure 7)

- Low pressure system so the assumption of ideal gas behaviour is reasonable
- Symmetric flow conditions and geometry along the foam centre plane (r = 0)

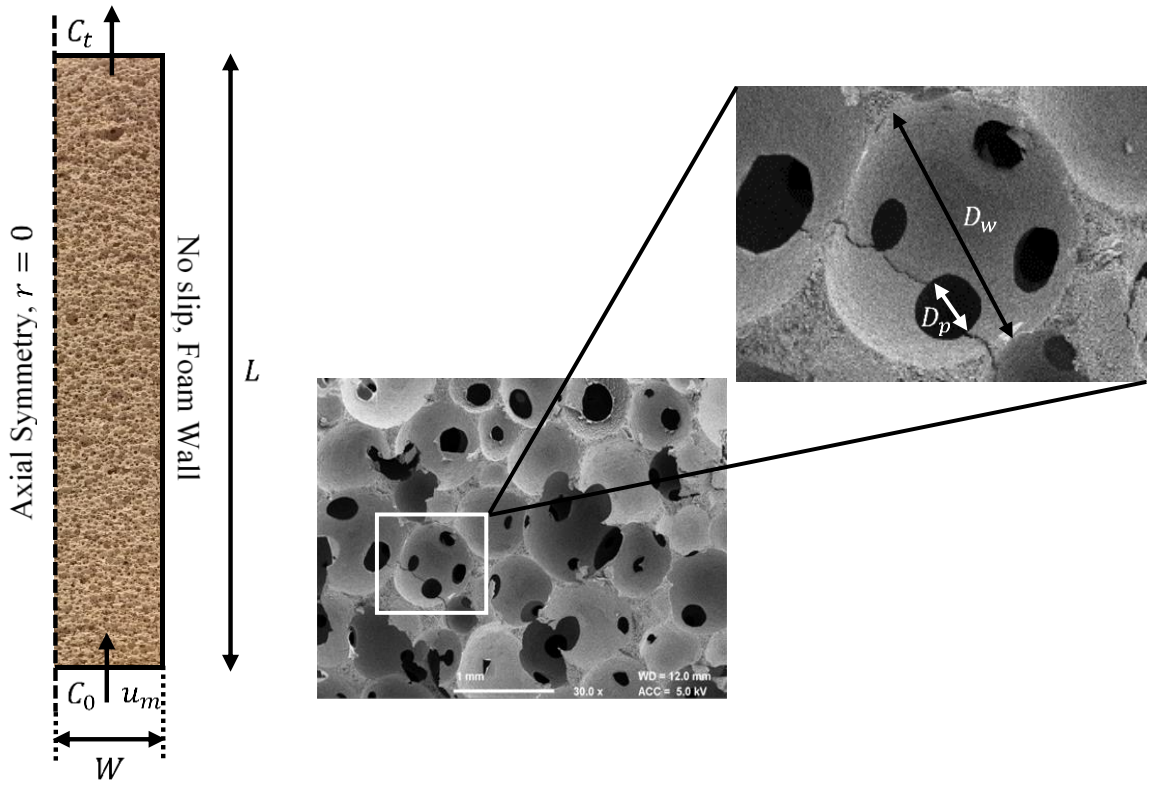

(a) (b)

Figure 9: (a) 2-D axisymmetric computational domain approximating the porous domain, labelled with CO_2 concentrations and velocities (L = 0.27 m , W = 0.0185 m), (b) scanning electron microscopy (SEM) micrograph of the PI/13X foam surface, $D_w = (8 \pm 1.5) \times 10^{-4}\ m$, $D_p = (2 \pm 0.8) \times 10^{-4}\ m$.

Table 4: Model Parameters.

Parameter	Definition	Value	Unit	Source/Equations
D	Diameter of foam	0.037	m	Experimental data
L	Length of foam	0.27	m	Experimental data (Total length of 3 foams)
W	Radius of foam	0.0185	m	Experimental data

D_p	Pore diameter		2.01×10^{-4}	m	Average of 10 readings taken from Figure 9 (b)
D_w	Pore-window diameter		8.11×10^{-4}	m	Average of 10 readings taken from Figure 9 (b)
η	Cell ratio		0.969		Equation 11
ε_p	Foam voidage		0.55 – 0.6		Measured experimentally using a saturation method [47]
k'_K	Modified Kozeny constant		0.822		Equation 12, For ε_p of 0.6
A'	Coefficient for calculating k'_K		13.3		[48], For ε_p of 0.6
K	Permeability of porous domain		1.09×10^{-9}	m^2	Equation 13, For ε_p of 0.6
Re_m	Modified Reynolds Number		0.47 – 0.52		Equation 6, For ε_p of 0.55 – 0.6
Pe	Peclet Number		276 - 286		Equation 7, For ε_p of 0.55 – 0.6
Sc	Schmidt Number		0.70		Equation 7
k_L	Langmuir constant	0k PVP	1.89	$m^3\ mol^{-1}$	Equation 15, Equation 16
		10k PVP	2.17		
		40k PVP	2.06		
		58k PVP	1.97		
q_{max}	Maximum adsorption capacity	0k PVP	0.00206	mol CO_2 g^{-1} 13X	Equation 15, Equation 16
		10k PVP	0.00211		
		40k PVP	0.00188		
		58k PVP	0.00224		

ρ_b	Bulk density	174 – 195	kg m^{-3}	Determined using foams
ρ_p	PI density	1300	kg m^{-3}	Taken from COMSOL Multiphysics 5.3
D_{CO_2}	CO_2 diffusion coefficient	1.06×10^{-5}	m^2 s^{-1}	[49]
ρ_f	Density of CO_2	1.98	kg m^{-3}	[50]
μ_f	Viscosity of CO_2	1.47×10^{-5}	Pa s	[51]
Q	Flow rate of CO_2	8.33×10^{-6}	m^3 s^{-1}	Experimental data, converted from mL min^{-1}
u_m	Mean fluid velocity	0.00775	m s^{-1}	
u_{max}	Maximum fluid velocity	0.0155	m s^{-1}	Determined by taking 2 times u_m
C_0	Initial CO_2 concentration	1.66	mol m^{-3}	Experimental data, converted from 40000 ppmv
P	Pressure	101325	Pa	Experimental data
T	Temperature	293.15	K	Experimental data

4.2 Governing Equations

Continuity Equation:

The adsorptive gas (CO_2 in air) was assumed to be ideal and the gas flow was treated as Newtonian. Since the operating pressure is 101325 Pa, it is reasonable to assume that the gas is incompressible. The continuity equation can be written as:

$$\nabla \cdot \boldsymbol{u} = 0 \qquad (5)$$

where $\boldsymbol{u}$ is the velocity vector.

Energy losses in the foam system can be due to viscous and form drags. The energy loss is significantly affected by the flow regime and also the foam structure i.e. voidage [52]. The modified Reynolds number, Re_m was used to characterise the flow regime [48]:

$$Re_m = \frac{\rho_f u_m D_p}{\mu_f(1-\varepsilon_p)} \quad (6)$$

where u_m is superficial velocity, ρ_f is density of CO_2, D_p is pore diameter, μ_f is viscosity of CO_2, ε_p is foam voidage. The voidage was determined experimentally by a saturation method demonstrated by Safiuddin and Hearn [47]. Re_m values ranged from 0.47 – 0.52, for ε_p values ranging from 0.55 – 0.6. Hence, for the model it was confirmed the flow regime was laminar [52]. The Peclet number was used to determine the significance of convection/diffusion in the distribution of CO_2 in the foam [53]:

$$Pe = \frac{u_m L}{D_L} \quad (7)$$

where $D_L = \frac{[0.23+0.5ScRe_m]D_{CO_2}}{\varepsilon_p}$ and the Schmidt number, $Sc = \frac{\mu_f}{\rho_f D_{CO_2}}$, Pe is Peclet number, L is length of foam, D_L is axial dispersion coefficient, D_{CO_2} is diffusion coefficient of CO_2. Using Equation 7, the Peclet number ranged from 276 – 286, for ε_p values ranging from 0.55 – 0.6. Since Pe is significantly large, convection dominates the transport of CO_2.

Conservation of momentum (Brinkman equations):

The Brinkman equation as shown in Equation 8, was used to describe the fluid flow in the porous domain due to the presence of large pores. It is a mathematical model extended from Darcy's law which accounts for viscous effects in bulk. The Brinkman equation can be written as [54]:

$$\rho_f\left(\frac{\partial \boldsymbol{u}}{\partial t}\right) = -\nabla P + \nabla\left[\frac{\mu_f}{\varepsilon_p}\{\nabla \boldsymbol{u} + (\nabla \boldsymbol{u})^T\}\right] - \left(K^{-1}\mu_f\right)\boldsymbol{u} \quad (8)$$

where t is time, K is permeability.

Permeability, K depends on the structure of the porous matrix and is independent of the properties of the fluid [55]. The main parameters which affect permeability are porosity, pore shape and the connectivity of pores with one another [55]. Since the flow is laminar, the Carman-Kozeny permeability

model was used in an attempt to link the permeability factor to ε_p in the model. However, this model was primarily developed for packed beds of spherical particles [48]. Since porosity and pore size vary significantly in foams compared to packed beds of spherical particles, it was necessary to modify the Carman-Kozeny permeability model for foams. The modified model was based on a geometry model with interconnected sphere-centred cubes, where the interconnected spheres represented the void phase of the porous media. Karimian and Straatman [48] used the dimensions of the unit cube geometry to calculate the cell ratio, η and this in turn was used to calculate D_p. This can be seen in Equations 9 and 10.

$$\eta = \frac{H}{D_w} \tag{9}$$

where η is cell ratio, H is cell size, D_w is pore-window diameter

$$D_p = \left[\sqrt{(1-\eta^2)}\right] \times D_w \tag{10}$$

Since D_w and D_p were determined from SEM images as shown in Figure 9 (b), Equation 10 was rearranged to give Equation 11 for calculating the cell ratio.

$$\eta = \sqrt{1 - \left(\frac{D_p}{D_w}\right)^2} \tag{11}$$

The Kozeny constant in the model includes the effects of tortuosity, particle shape and their connections [55]. The constant is usually approximated as 5 for packed beds but varies strongly with porosity for other internal structures [48]. Therefore, the Kozeny constant was modified by incorporating a coefficient which varies with porosity. This can be seen in Equation 12. The modified Kozeny constant was adapted using a 'coefficient-porosity' correlation reported by Karimian and Straatman for foams [48]:

$$k_K^{'} = (1-\eta^2) \times A^{'} \tag{12}$$

where $k_K^{'}$ is modified Kozeny constant, $A^{'}$ is a coefficient which varies with porosity for calculating $k_K^{'}$.

With the calculated modified Kozeny constant and the cell ratio, permeability of the porous matrix can be determined as a function of porosity. The permeability as a function of porosity can be written as [48]:

$$K = \frac{D_p^2 \varepsilon_p^3 \eta^6}{k_K' \pi^2 (3\eta - 2)^2} \quad (13)$$

Initial and boundary conditions (variables are defined in Table 4):

- Foam wall: No-slip, When $r = W, u_z = 0$
- Foam inlet: Flow is fully developed and velocity profile is parabolic due to laminar flow, When $z = 0, u_z = u_{max}\left[1 - \left(\frac{r}{W}\right)^2\right]$
- Foam outlet: Operating pressure (101325 Pa) has been indicated in the model and so, When $z = L, P = 0\ Pa$
- Initial conditions: When $t = 0, P = 0\ Pa$ and $u_z = 0$

Species transport and adsorption (mass balance equations):

The species balance equation for CO_2 can be written as:

$$\left(\varepsilon_p + \rho_b k_L\right)\frac{\partial C}{\partial t} + \left(C - \rho_p q_{eq}\right)\frac{\partial \varepsilon_p}{\partial t} + \boldsymbol{u} \cdot \boldsymbol{\nabla} C = \nabla \cdot [(D_D + D_e)\boldsymbol{\nabla} C] \quad (14)$$

$$q_{eq} = \frac{q_{max} k_L C}{1 + k_L C} \quad (15)$$

Linear form of Langmuir isotherm:

$$\frac{C}{q_{eq}} = \frac{1}{q_{max}} C + \frac{1}{q_{max} k_L} \quad (16)$$

where $D_e = \frac{\varepsilon_p}{\tau_f} D_{CO_2}$ and the tortuosity factor (Millington and Quirk Model), $\tau_f = {\varepsilon_p}^{-\frac{1}{3}}$, ρ_b is bulk density, k_L is Langmuir constant, C is concentration of CO_2, ρ_p is polyimide density, q_{eq} is equilibrium adsorption capacity, D_D is dispersion tensor of CO_2, D_e is effective diffusion coefficient of CO_2, τ_f is tortuosity factor, q_{max} is maximum adsorption capacity.

The governing equation for the adsorptive mass balance assumed that the foams consist of uniformly distributed immobile 13X zeolite particles. On the left-hand side of Equation 14, the first two terms describe the accumulation of CO_2 via adsorption in the polymeric matrix. Since the foams are assumed to be isotropic, porosity is uniform throughout the foam and constant. The third term describes the movement of CO_2 through the pore channels and this term incorporates the velocity vector [46]. The Langmuir isotherm (Equation 15) was used to predict the concentration of CO_2 adsorbed onto and desorbed from the 13X zeolite surface [56]. Using IGA data obtained from the actual PI/13X foams and Equation 16, k_L and q_{max} were determined by plotting a linear Langmuir isotherm. The R^2 value obtained from the trendline for all the PI/13X foam samples was 0.996. Lastly, the dispersion and diffusion term on the right hand side of Equation 14, include the self-induced movement of CO_2 within the pore spaces [46]. There were no reaction and source terms as there are no products being produced and no reactants being consumed.

Initial and boundary conditions (variables are defined in Table 4):

- Foam wall: No flux, When $r = W, C = 0$
- Foam inlet: Inlet concentration of adsorptive gas, When $z = 0, C = C_0$
- Foam outlet: Gas flux dominated by convection, When $z = L, C = C_t$ and $-\boldsymbol{n}\left(D_{CO_2}\nabla C\right) = 0$
- Initial conditions: No adsorptive in the foam system and adsorbent was free of adsorptive, When $t = 0, C = 0$ and $q_{eq} = 0$

4.3 Meshing and convergence tests

The computation domain was approximated using unstructured triangular elements or meshes, as shown in Figure 10 (a) and (b). The density of meshes was increased in the area where the velocity gradient is maximum (i.e. the region near the wall). The convergence criteria in all simulations were set to 10^{-2}. Several diagnostic tests were performed to ensure the accuracy of the solutions. In one, the number of iterations for one of the simulation runs was increased by 50%: the solution did not drift away from the converged result. In the second, the number of elements used in the simulation was varied using different degrees of mesh refinement to determine when mesh dependency had been eliminated. Figure

10 (c) shows that the concentration of CO_2 was independent of the number of elements from approximately 30000 and this was the finer mesh setting in COMSOL. This was employed for all simulations.

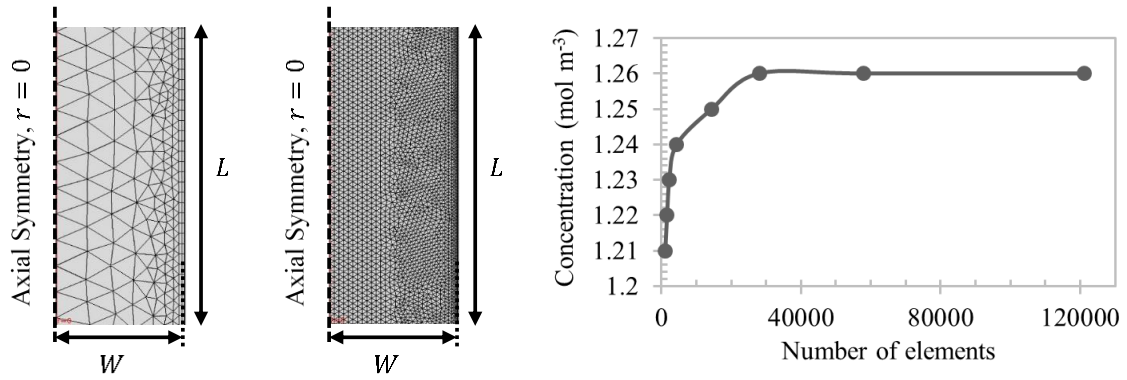

(a) (b) (c)

Figure 10: (a) Coarser (2269 elements) mesh distribution, (b) Finer (~30000 elements) mesh distribution, (c) CO_2 concentration at 50% of foam length for varying mesh distribution.

4.4 Results and discussions

The comparison of 4% vol. CO_2 in air dynamic adsorption breakthrough curves for 10k, 40k and 58k PVP adsorbent foams and the modelled breakthrough curves are shown in Figure 11 (a) – (d). Figure 11 shows that for all the PVP molar masses, the model breakthrough curves were S-shaped, similar to the experimental breakthrough curves. The 300-10k model curve was the most accurate compared to the experimental curve as seen in Figure 11 (b). 300-58k (Figure 11 (d)) model curve was the least accurate compared to the experimental curve. The experimental breakthrough time observed for both 300-0k (Figure 11 (a)) and 300-40k foams (Figure 11 (c)), were slightly longer compared to the corresponding model breakthrough time.

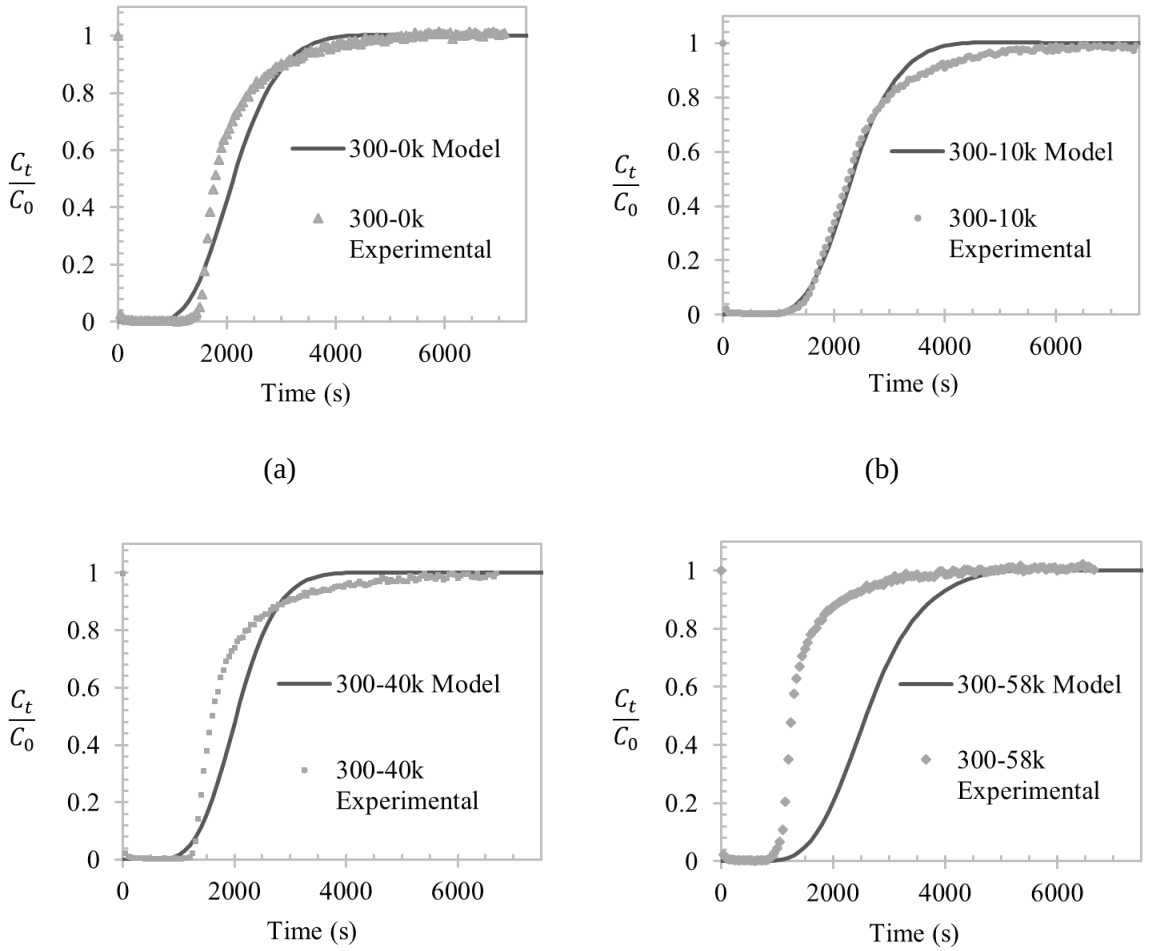

Figure 11: 4% vol. CO_2 Experimental and Model breakthrough curve at 293.15K, 101325 Pa and a flow rate of 500 mL min^{-1} for (a) 300-0k, (b) 300-10k, (c) 300-40k, (d) 300-58k.

The experimental results show that the dynamic adsorption breakthrough curve for the foam prepared using the 58k PVP pore former is much broader than the curves for the foams prepared with 10k PVP and 40k PVP respectively. This implies that the foam prepared using a higher molecular weight pore former has a much poorer kinetic performance than the 10k PVP foams of the same material. Since the model uses the equilibrium isotherm data compared to the dynamic experimental data, high mass transfer resistances experienced in 300-58k is not reflected in the predicted breakthrough curve. Table 5 shows the comparison of the equilibrium loading obtained from the simulation and the experimental

breakthrough curves. Equation 1 was used to determine the equilibrium loading from the simulated breakthrough curves.

Table 5: Equilibrium loading calculated from simulated breakthrough curves for 300-0k, 300-10k, 300-40k and 300-58k foams challenged with 4% vol. CO_2 in Air.

Sample	Experimental $q_{eq}\left(\frac{g\ CO_2}{g\ 13X}\right)$	Predicted $q_{eq}\left(\frac{g\ CO_2}{g\ 13X}\right)$	Difference for q_{eq} (%)
300-0k	0.032 ± 6.4%	0.036	+11%
300-10k	0.039	0.037	-5%
300-40k	0.029	0.032	+9%
300-58k	0.021	0.039	+46%

Table 5 shows that the predicted q_{eq} values for 300-0k, 300-10k and 300-40k are in good agreement with the experimental q_{eq} values as the difference was calculated to be less than 11%. However, 300-58k had the highest percentage difference of 46% between the predicted and experimental q_{eq} values. This could have possibly been due to the simulation not considering the effect of PVP masking the zeolite surface. As mentioned in Section 3.3, the higher the PVP molar mass, the more difficult it would be to remove it. It is evident in Figure 11 and Table 5 that the effect of PVP masking the zeolite surface is more significant for PVP molar mass higher than 40k. Therefore, the predicted adsorption capacity of 300-58k was higher compared to the experimental adsorption capacity.

During an adsorption experiment, it is difficult to visualize the movement of the mass transfer zone (MTZ) throughout the foam axially and radially. However, with modelling, the movement of the MTZ can be obtained to elucidate the shape of the breakthrough curve. Since the 300-10k model data had the best match with the experimental data, the progression of the MTZ for the model breakthrough curve (Figure 11 (b)), was simulated as seen in Figure 12.

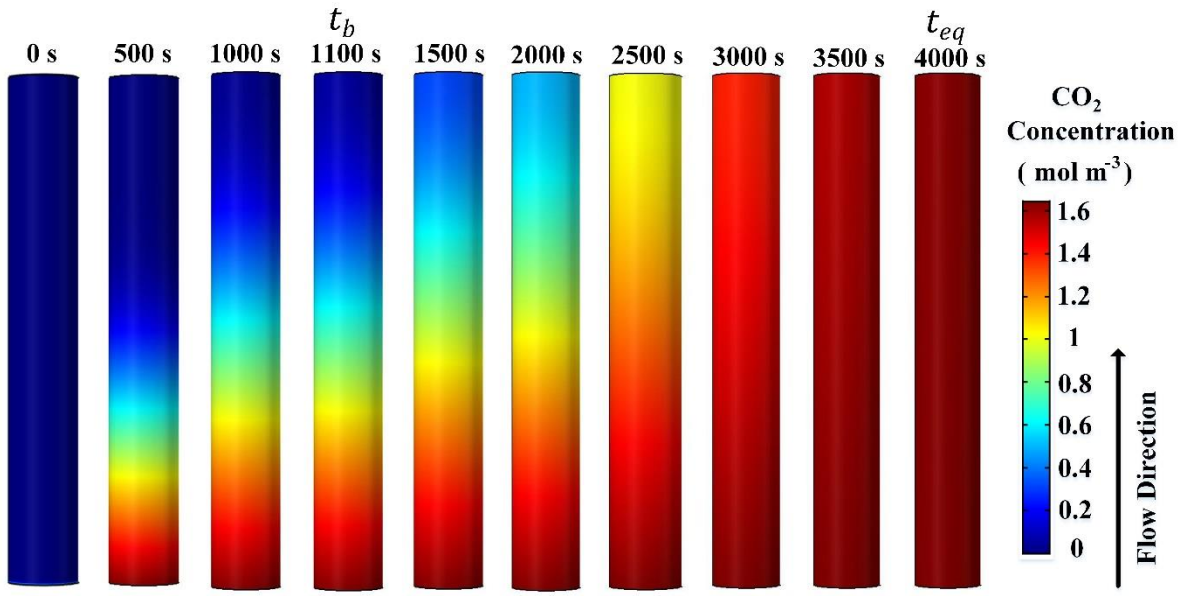

Figure 12: CO_2 distribution throughout the full (L = 0.27 m, W = 0.0185 m) adsorbent foam column (300-10k) at different time points at 101325 Pa and 293.15 K for a flow rate of 500 mL min^{-1}; t_b – breakthrough time, t_{eq} – equilibrium time.

Figure 12 shows the CO_2 concentration at the foam outlet at 1100 s, was approximately 0.1 mol m^{-3} (1% of the inlet concentration) and thus indicating that breakthrough had occurred. This matches with the experimental observation shown in Figure 11 (b). Both the experimental data and simulation results also show that the adsorbent foam was exhausted and had reached equilibrium at approximately 4000 s. The effect of initial CO_2 concentration on the breakthrough performance of the 300-10k foam can be predicted using the validated model as shown in Figure 13 (a). As expected, the increase in CO_2 concentration results in a sharper breakthrough curve (Figure 13 (a)) and a higher equilibrium loading (Figure 13 (b)). The simulation can also be used for predicting the adsorption performance of the foams for multiple gas species or a different adsorptive gas.

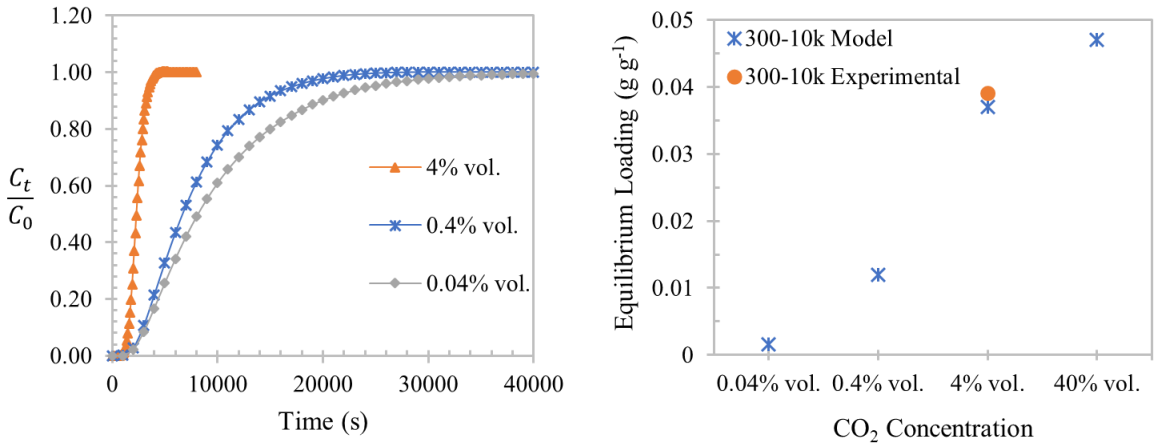

(a) (b)

Figure 13: (a) 300-10k model breakthrough curves obtained by varying initial CO_2 concentration, (b) Predicted and actual effect of initial CO_2 concentration on equilibrium loading for 300-10k.

Figure 14 shows the pressure drop of the 300-0k foam, packed bed filled with 0.4 – 0.8 mm beads (bed A) and 1.0 – 1.6 mm beads (bed B), all determined experimentally.

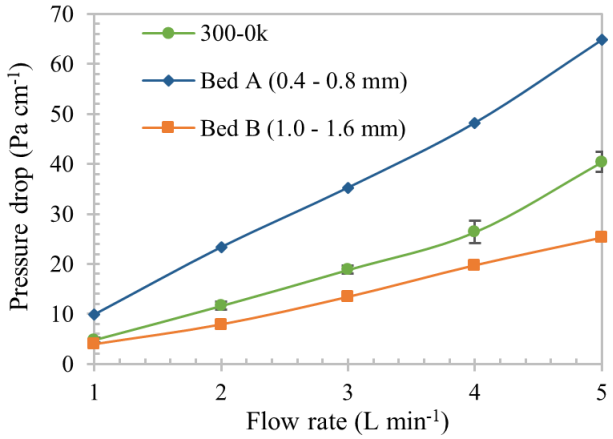

Figure 14: Experimental pressure drop data for 300-0k adsorbent foam compared with packed bed A (0.4 – 0.8 mm) and packed bed B (1.0 – 1.6 mm).

Figure 14 shows that as the flow rate increases, the difference in pressure drop between the foam, bed A and bed B become significant. Experimental data shows that the pressure drop in the foam was lower than the 0.6mm (average) bead beds. However, the design of the foam bubble/pore windows, and pressure drop will require further optimisation by using CFD modelling. Several combinations of parameters can be tested using the model to find the best set of parameters that give a good adsorption performance whilst reducing pressure drop, without having to physically prepare the foams.

5 Conclusions

Foams containing 80 wt% 13X/20 wt% Polyimide (PI) were successfully fabricated using a new generic synthesis method comprising of a dual parallel reaction foaming process, which consists of a CO_2 generation (blowing) reaction and a polymerisation reaction. Three molecular weights of polyvinylpyrrolidone (PVP) namely, 10k, 40k and 58k, were used as pore-formers to enable more exposure of adsorption sites to contaminants. The adsorbent foam produced with 10k PVP was found to be superior in quality in terms of uniform pore size, better adsorption capacity, and improved kinetic performance than foams produced from either of the other two PVPs. The adsorbent foam with 10k PVP also featured the best breakthrough and equilibrium times for CO_2. Isotherm data obtained using an Intelligent Gravimetric Analysis (IGA) confirmed that the adsorption capacity of the foam sample increased with pressure and the presence of 20 wt% PI in the foam had only slight impact on CO_2 adsorption.

The morphology and adsorption properties of the foam were found to be mainly dependent on the quantity of water used, the ratio of adsorbent to polymer composition, and the pretreatment temperatures of zeolites. The bubble skin-pore structure of the 13X foams seems to be largely determined by the water content and type of PVP used. Since the foams have highly open porous structures with a small skin thickness in bubbles, they are expected to have minimal mass transfer resistance during molecular transport processes. Heat treatment influenced not only the morphology but also the adsorption/separation performance of the foams. The adsorption-regeneration cycles indicated that the CO_2 breakthrough time increased until equilibrium was reached. Thermal analysis of the pure PI and 13X showed that these materials were stable up to 400°C. It is concluded that the optimum heat treatment conditions for PI/13X foams is 300ºC.

Computational simulations were successfully conducted to elucidate the concentration profiles of CO_2 within the foams. The breakthrough profiles for 300-10k foams were successfully verified by experimental data but the 300-58k data showed significant discrepancies. This may be a result of the presence of PVP masking the zeolite surface and not being reflected in the simulation. Further investigations will be required to confirm this observation.

It is possible to conclude that the combined effects of suitable polymer/zeolite/additives composition and reasonable heat treatment can produce foams which have superior quality for pollution control applications. These results augur well for the adsorbent foam composite systems. With such composite foam structure, it is anticipated that compact, light-weight, low pressure drop devices could be constructed for a range of applications including CO_2 recovery, volatile organic compound (VOC) removal, gas separation, and wastewater treatment, etc.

6 Appendices

Appendix A: TG Blank Test

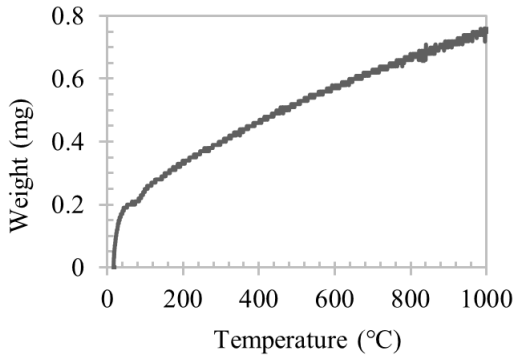

Figure A. 1: TG curve for empty alumina crucible.

Acknowledgements

Ramya G would like to thank University of Bath for the University Research Studentship. The authors gratefully acknowledge the technical assistance provided by Fernando Acosta, Cassie Reis and Clare Bell in the Department of Chemical Engineering at the University of Bath. Also, for the assistance provided by Mr Philip Fletcher for using the scanning electron microscopy (SEM) at the Microscopy and Analysis Suite (MAS) was acknowledged.

References

[1] W.J. Thomas, B. Crittenden, Adsorbents, in: Adsorpt. Technol. Des., Butterworth-Heinemann, London, 1998: p. 14.

[2] D.M. Ruthven, C. Thaeron, Performance of a parallel passage adsorbent contactor, Gas, Sep. Purif. 10 (1996) 63–73.

[3] F. Akhtar, L. Andersson, S. Ogunwumi, N. Hedin, L. Bergström, Structuring Adsorbents and Catalysts by Processing of Porous Powders, J. Eur. Ceram. Soc. 34 (2014) 1643–1666.

[4] X. Feng, C.Y. Pan, C.W. McMinis, J. Ivory, D. Ghosh, Hollow-fiber-based adsorbers for gas separation by pressure swing adsorption, AIChE J. 44 (1998) 1555–1562.

[5] G.L. Gilleskie, J.L. Parker, E.L. Cussler, Gas separations in hollow-fiber adsorbers, AIChE J. 41 (1995) 1413–1425.

[6] F. Rezaei, P. Webley, Structured adsorbents in gas separation processes, Sep. Purif. Technol. 70 (2010) 243–256.

[7] S.G. Li, G.H. Koops, M.H.V. Mulder, T. Van Den Boomgaard, C.A. Smolders, Wet spinning of integrally skinned hollow fiber membranes by a modified dual-bath coagulation method using a triple orifice spinneret, J. Memb. Sci. 94 (1994) 329–340.

[8] F. Rezaei, P. Webley, Optimum structured adsorbents for gas separation processes, Chem. Eng. Sci. 64 (2009) 5182–5191.

[9] Y.Y. Li, S.P. Perera, B.D. Crittenden, Zeolite Monoliths for Air Separation, Chem. Eng. Res. Des. 76 (1998) 921–930.

[10] J.M. Nevell, S.P. Perera, Novel adsorbent hollow fibres for oxygen concentration, Adsorption. 17 (2011) 273–283.

[11] J.T. Richardson, Y. Peng, D. Remue, Properties of ceramic foam catalyst supports: pressure drop, Appl. Catal. A Gen. 204 (2000) 19–32.

[12] T.S. Chung, L.Y. Jiang, Y. Li, S. Kulprathipanja, Mixed matrix membranes (MMMs) comprising organic polymers with dispersed inorganic fillers for gas separation, Prog. Polym.

Sci. 32 (2007) 483–507.

[13] K.-B. Yoon, Y.-J. Lee, Y.-S. Park, J.-S. Lee, Macroporous foams comprising microporous zeolite or zeotype material and preparation thereof by using polymeric templates having sponge structure, 148,780, 2002.

[14] P. Liu, G.-F. Chen, Applications of Porous Ceramics, in: Porous Mater. Process. Appl., Elsevier Ltd, United Kingdom, 2014: pp. 341–342.

[15] A. Buekenhoudt, A. Kovalevsky, J. Luyten, F. Snijkers, Basic Aspects in Inorganic Membrane Preparation, in: Compr. Membr. Sci. Eng., Elsevier, 2010: pp. 217–252.

[16] S.V. Vinogradova, Y.S. Vygodskii, V.V. Korshak, Some features of the synthesis of polyimides by single-stage high-temperature polycyclization, Polym. Sci. U.S.S.R. 12 (1970) 2254–2262.

[17] C.S. Marvel, Thermally stable polymers, Pure Appl. Chem. 16 (1968) 351–368.

[18] X.-Y. Liu, M.-S. Zhan, K. Wang, Y. Li, Y.-F. Bai, Preparation and performance of a novel polyimide foam, Polym. Adv. Technol. 23 (2011) 677–685.

[19] N.S. Trouw, Process for the production of polybenzimidazole foams, 791,049, 1986.

[20] W.J. Koros, G.K. Fleming, S.M. Jordan, T.H. Kim, H.H. Hoehn, Polymeric membrane materials for solution-diffusion based permeation separations, Prog. Polym. Sci. 13 (1988) 339–401.

[21] D.J. Liaw, K.L. Wang, Y.C. Huang, K.R. Lee, J.Y. Lai, C.S. Ha, Advanced polyimide materials: Syntheses, physical properties and applications, Prog. Polym. Sci. 37 (2012) 907–974.

[22] M.K. Ghosh, K.L. Mittal, Synthesis of Polyimides, in: Polyimides Fundam. Appl., Marcel Dekker, New York, 1996: p. 40.

[23] C. Defonseka, Properties and Foaming Technology of Polyurethane Foam, in: Pract. Guid. to Flex. Polyurethane Foam., Smithers Rapra, United Kingdom, 2013: p. Pract. Guid. to Flex. polyurethane Foam.

[24] A. Aneja, Structure-Property Relationships of Flexible Polyurethane Foams, Virginia Polytechnic Institute and State University, 2002.

[25] A. Sarkar, Synthesis and Characterization of Polyamides, Polyimides and Polyesters Containing Flexibilizing Groups, University of Pune, 2005.

[26] C. Tien, Fixed-Bed Adsorption Calculations, in: Adsorpt. Calc. Model., Butterworth-Heinemann, New York, 1994: p. 123.

[27] Honeywell UOP, An Introduction to Zeolite Molecular Sieves, (n.d.) 8. http://www.petrotex.us/wp-content/uploads/2013/04/UOP-Manual.pdf.

[28] C. Zhou, A. Alshameri, C. Yan, X. Qiu, H. Wang, Y. Ma, Characteristics and evaluation of synthetic 13X zeolite from Yunnan's natural halloysite, J. Porous Mater. 20 (2013) 587–594.

[29] F. Yu, K. Wang, X.-Y. Liu, M.-S. Zhan, Preparation and Properties of Rigid Polyimide Foams Derived from Dianhydride and Isocyanate, J. Appl. Polym. Sci. 127 (2012) 5075–5081.

[30] Y. Kim, H. Park, Y. Lee, Gas separation properties of carbon molecular sieve membranes derived from polyimide/polyvinylpyrrolidone blends: effect of the molecular weight of polyvinylpyrrolidone, J. Memb. Sci. 251 (2005) 159–167.

[31] H. Matsuyama, T. Maki, M. Teramoto, K. Kobayashi, Effect of PVP Additive on Porous Polysulfone Membrane Formation by Immersion Precipitation Method, Sep. Sci. Technol. 38 (2007) 3449–3458.

[32] Y. Park, Y. Ju, D. Park, C.H. Lee, Adsorption equilibria and kinetics of six pure gases on pelletized zeolite 13X up to 1.0 MPa: Carbon dioxide, Carbon monoxide, Nitrogen, Methane,

Argon and Hydrogen, Chem. Eng. J. 292 (2016) 348–365.

[33] L. Hauchhum, P. Mahanta, Carbon dioxide adsorption on zeolites and activated carbon by pressure swing adsorption in a fixed bed, Int. J. Energy Environ. Eng. 5 (2014) 349–356.

[34] J. Pires, V.K. Saini, M.L. Pinto, Studies on selective adsorption of biogas components on pillared clays: Approach for biogas improvement, Environ. Sci. Technol. 42 (2008) 8727–8732.

[35] H. Wei, S. Deng, B. Hu, Z. Chen, B. Wang, J. Huang, G. Yu, Granular Bamboo-Derived Activated Carbon for High Carbon Dioxide Adsorption: The Dominant Role of Narrow Micropores, ChemSusChem. 5 (2012) 2354–2360.

[36] J. Cai, J. Qi, C. Yang, X. Zhao, Poly(vinylidene chloride)-based carbon with ultrahigh microporosity and outstanding performance for Methane and Hydrogen storage and Carbon Dioxide capture, ACS Appl. Mater. Interfaces. 6 (2014) 3703–3711.

[37] X. Hu;, M. Radosz;, K.A. Cychosz;, M. Thommes;, Carbon Dioxide - Filling Capacity and Selectivity of Carbon Nanopores: Synthesis, Texture, and Pore-Size Distribution from Quenched-Solid Density Functional Theory (QSDFT), Environ. Sci. Technol. 45 (2011) 7068–7074.

[38] J. Wang, A. Heerwig, M.R. Lohe, M. Oschatz, L. Borchardt, S. Kaskel, Fungi-based porous carbons for carbon dioxide adsorption and separation, J. Mater. Chem. 22 (2012) 13911–13913.

[39] J. Wang, I. Senkovska, M. Oschatz, M.R. Lohe, L. Borchardt, A. Heerwig, Q. Liu, S. Kaskel, Highly Porous Nitrogen-doped Polyimine-based Carbons with Adjustable Microstructures for Carbon Dioxide Capture, J. Mater. Chem. A. 1 (2013) 10951–10961.

[40] C. Chen, Y. Yu, C. He, L. Wang, H. Huang, R. Albilali, J. Cheng, Z. Hao, Efficient capture of carbon dioxide over ordered micro-mesoporous hybrid carbon nanosphere, Appl. Surf. Sci.

439 (2018) 113–121.

[41] C. Chen, H. Huang, Y. Yu, J. Shi, C. He, R. Albilali, H. Pan, Template-free synthesis of hierarchical porous carbon with controlled morphology for carbon dioxide efficient capture, Chem. Eng. J. 353 (2018) 584–594.

[42] T. Chen, S. Deng, B. Wang, J. Huang, Y. Wang, G. Yu, Carbon Dioxide Adsorption on Crab Shell Derived Activated Carbons: Contribution of Micropores and Nitrogen-Containing Groups, RSC Adv. 5 (2015) 48323–48330.

[43] C. Zhang, W. Song, Q. Ma, L. Xie, X. Zhang, H. Guo, Enhancement of Carbon Dioxide Capture on Biomass-Based Carbon from Black Locust by KOH Activation and Ammonia Modification, Energy and Fuels. 30 (2016) 4181–4190.

[44] K. Li, S. Tian, J. Jiang, J. Wang, X. Chen, F. Yan, Pine cone shell-based activated carbon used for carbon dioxide adsorption, J. Mater. Chem. A. 4 (2016) 5223–5234.

[45] J. Kou, L.-B. Sun, Fabrication of Nitrogen-Doped Porous Carbons for Highly Efficient Carbon Dioxide Capture: Rational Choice of a Polymer precursor, J. Mater. Chem. A. 4 (2016) 17299–17307.

[46] D.T. Tefera, M.J. Lashaki, M. Fayaz, Z. Hashisho, J.H. Philips, J.E. Anderson, M. Nichols, Two-Dimensional Modeling of Volatile Organic Compounds (VOCs) adsorption onto beaded activated carbon, Environ. Sci. Technol. 47 (2013) 11700–11710.

[47] M. Safiuddin, N. Hearn, Comparison of ASTM saturation techniques for measuring the permeable porosity of concrete, Cem. Concr. Res. 35 (2005) 1008–1013.

[48] S.A.M. Karimian, A.G. Straatman, CFD study of the hydraulic and thermal behavior of spherical-void-phase porous materials, Int. J. Heat Fluid Flow. 29 (2008) 292–305.

[49] I.L. Mostinsky, Diffusion Coefficient, (2011). http://www.thermopedia.com/content/696/

(accessed August 2, 2017).

[50] The Engineering ToolBox, Gases - Density, (n.d.). https://www.engineeringtoolbox.com/gas-density-d_158.html (accessed August 1, 2017).

[51] The Engineering ToolBox, Gases - Dynamic Viscosity, (n.d.). https://www.engineeringtoolbox.com/gases-absolute-dynamic-viscosity-d_1888.html (accessed August 2, 2017).

[52] A. Dybbs, R.V. Edwards, A new look at porous media fluid mechanics - Darcy to turbulent, in: Fundam. Transp. Phenom. Porous Media, Martinus Nijhoff, Dordrecht, 1984: p. 204.

[53] T.L.P. Dantas, F.M.T. Luna, I.J. Silva Jr, A.E.B. Torres, D.C.S. de Azevedo, A.E. Rodrigues, R.F.P.M. Moreira, Modeling of the Fixed-Bed Adsorption of Carbon Dioxide and a Carbon Dioxide-Nitrogen Mixture on Zeolite 13X, Brazilian J. Chem. Eng. 28 (2011) 533–544.

[54] D.A. Nield, A. Bejan, Mechanics of Fluid Flow through a Porous Medium, in: Convect. Porous Media, Third, Springer Science+Business Media Inc., United States of America, 2006: p. 4.

[55] T. Ozgumus, M. Mobedi, U. Ozkol, Determination of Kozeny Constant Based on Porosity and Pore to Throat Size Ratio in Porous Medium with Rectangular Rods, Eng. Appl. Comput. Fluid Mech. 8 (2014) 308–318.

[56] X. Chen, Modeling of Experimental Adsorption Isotherm Data, Inf. 6 (2015) 14–22.